PAPER

Check for updates

A bismuth silver pnictohalide alternative to perovskite in fully-printable triple-mesoscopic solar cells†

Ying Yuan and Neil Robertson [iD] *

Recent Ag$_3$BiI$_6$ solar cells have demonstrated promising efficiency, however, most have focused on mesoporous n-i-p configuration, using expensive hole transport materials (*e.g.*, P3HT, PTAA and spiro-OMeTAD) and a Au counter electrode. To lower the cost and potentially enable larger scale Ag$_3$BiI$_6$ solar cells, herein, this study provides the first feasibility examination of Ag$_3$BiI$_6$ in fully-printable triple-mesoscopic (TiO$_2$/ZrO$_2$/carbon) solar cells (TM-SCs) and explores the effect of pre-treatment with small molecules and post-treatment (CuSCN) on the overall Ag$_3$BiI$_6$ TM-SC performance. An Ag$_3$BiI$_6$ solar cell with a power conversion efficiency (PCE) of 0.38% ($J_{sc} = 1.97$ mA cm^{-2}; $V_{oc} = 0.49$ V; fill factor = 0.39) is demonstrated under 1 sun irradiation with two-month dark-storage stability in the ambient atmosphere. An improved V_{oc} from 0.43 V to 0.48 V was observed with biPY pre-treatment; a champion PCE of 0.74% ($J_{sc} = 2.78$ mA cm^{-2}; $V_{oc} = 0.56$ V; fill factor = 0.48) was achieved with CuSCN post-treatment. The results reported here represent a step toward developing all inorganic Bi-based absorbers in printable TM-SCs, suggesting that further improvements should be possible with porous surface engineering and efficient charge extraction.

1 Introduction

With the rapid development of perovskite solar cells (PSCs), the path to commercialisation is underway. The current fabrication technologies for highly-efficient PSCs, however, require quality perovskite layers to achieve outstanding performance, which is difficult to satisfy in large-scale manufacturing. Printable triple-mesoscopic solar cells (TM-SCs) opened a new chapter of PSCs with promising power conversion efficiency (PCE) up to 16.53%, which meets the scale-up commercialisation requirements, such as low cost and easy fabrication.[1–3] TM-SCs consist of mesoporous TiO$_2$ and ZrO$_2$ layers covered with a porous carbon film. Unlike the conventional PSCs, the TM-SCs can be fabricated by screen-printing, and the device can be filled with the perovskite by drop-casting. However, absorber filling of TM-SCs relies on spontaneous precursor diffusion and solvent evaporation, facing the challenge of unpredictable precursor penetration and crystallisation within pores, potentially introducing defects and recombination routes. To enhance the perovskite crystal growth and to regulate crystal kinetics, Han's group employed stabilisers, such as 5-ammonium valeric acid iodide

School of Chemistry and EaStCHEM, University of Edinburgh, King's Building, David Brewster Road, Edinburgh, Scotland EH9 3FJ, UK. E-mail: s1779788@ed.ac.uk; neil. robertson@ed.ac.uk

† Electronic supplementary information (ESI) available: EM and EDS images, absorption spectra, XPS survey spectra, *J–V* curve, energy alignment, dark storage stability and EIS. See DOI: https://doi.org/10.1039/d2se01324j

(5-AVAI) and 4-(aminomethyl) benzoic acid iodide (AB), improving the device performance from 7.2% to 14.1% and 15.6%, respectively.[1,4] Also, Xu *et al.* modified the porous surface of TM-SCs with a dye molecule, di-tetrabutylammonium *cis*-bis(isothiocyanato)bis(2,2′-bipyridyl-4,4′-dicarboxylato) ruthenium(II) (known as N719), and highlighted the passivation effect of N719@TiO$_2$ core–shell additives to suppress MA$^+$ vacancies and shallow defects. This facilitates charge separation, improving J_{sc} from 21.95 mA cm^{-2} to 23.58 mA cm^{-2}.[5,6] A similar approach has also been followed by other researchers using post-treatment, such as phenyl-C61-butyric acid methyl ester (PCBM) and copper thiocyanate (CuSCN) treatments, on perovskite TM-SCs to passivate the grain boundaries of perovskite and ease electron–hole pair separation.[7,8]

Despite the high efficiency achieved by PSCs, concerns have been raised over the stability and toxicity of lead-based perovskites. To address these issues, great interest has grown in Bi-based materials due to their non-toxicity and long-lasting stability. Silver pnictohalides (Ag–Bi–I) have attracted wide attention since 2016.[9–11] The controllable ratio of AgI to BiI$_3$ leads to varying compounds within this family, including AgBi$_2$I$_7$, AgBiI$_4$, Ag$_2$BiI$_5$ and Ag$_3$BiI$_6$, which have been extensively studied as light-absorbing materials.[9–15] The silver pnictohalide family shares similar 3D crystal structures and a suitable optical bandgap of 1.79–1.83 eV.[10] According to the ratio of Ag and Bi, they are classified into two space groups: $Fd\bar{3}m$ (AgBi$_2$I$_7$ and AgBiI$_4$) and $R\bar{3}m$ (Ag$_2$BiI$_5$ and Ag$_3$BiI$_6$).[16,17] Among the existing studies on silver pnictohalides, Ag$_3$BiI$_6$

stands out as a promising photovoltaic material. Although it is well known that AgI is insoluble in most organic solvents at room temperature, Turkevych et al. found that AgI is soluble in hot DMSO (110 °C) in the presence of BiI_3.[10] After dissolving AgI, the first solution-processed Ag_3BiI_6 solar cell was fabricated, demonstrating a promising PCE of 4.3%. After this, Pai et al. tailored the optical bandgap of Ag_3BiI_6 by partially substituting I^- by S^{2-}.[15] The modified compound, $Ag_3BiI_{5.92}S_{0.4}$, achieved a PCE of 5.44%, attributed to upshifting the valence band of Ag_3BiI_6. However, most studies of Ag_3BiI_6 devices have only focused on the mesoporous TiO_2-based configuration, namely FTO/compact-TiO_2 (c-TiO_2)/mesoporous-TiO_2 (m-TiO_2)/Ag_3BiI_6/HTM/Au, using expensive hole transport materials (HTMs) and Au electrodes. As TM-SCs arouse great interest in large-scale perovskite solar cell research, Li et al. first attempted to investigate Bi-based absorbers in this configuration.[18,19] However, Ag_3BiI_6 has not been previously studied in TM-SCs.

Inspired by the studies mentioned above, this paper explores the performance of Ag_3BiI_6 based TM-SCs and reveals the effect of specific pre-treatment and post-treatment on Ag_3BiI_6 devices. Fig. 1a shows the organic molecules applied in the device as pre-treatment: 4-tertbutylpyridine (4tBP), 2,2'-bipyridine (biPY), 4H-cyclopenta[2,1-b:3,4-b']dithiophene (CPDT-1) and N719. 4tBP and biPY are nitrogen-containing additives widely applied in dye-sensitised solar cells (DSSCs) to improve V_{oc}, where the lone-pair electrons of N attached to TiO_2 negatively shift the TiO_2 conduction band, leading to overall V_{oc} increase and surface hydrophobicity enhancement.[20,21] In perovskite solar cells, dye molecules have been reported previously as additives, bridging TiO_2 (by carboxyl group anchoring) with the perovskite and simultaneously passivating trap states (by the thioether group with uncoordinated metal cations).[5,6,22,23] Drawing upon two strands of pre-treatment research on solar cells, this paper compares two approaches, N-donor molecules (4tBP and biPY) and dye molecules (N719 and CPDT-1) to increase the wettability of the TiO_2 surface, and to improve the pore filling and device performance within TM-SCs. In addition, an HTM was included in the device to enhance hole extraction, mitigate potential imbalanced charge separation and reduce the hysteresis behaviour.[8,24] Although organic HTMs (e.g., poly(-triaryl amine), PTAA: poly(3-hexylthiophene-2,5-diyl), P3HT:

2,2',7,7'-tetrakis[N,N-di(4-methoxyphenyl)amino]-9,9'-spirobi-fluorene, and spiro-OMeTAD) are popular in conventional Ag_3BiI_6 devices, a cheaper alternative, CuSCN, with high hole mobility warrants an attempt in TM-SCs.[25,26] The study presented here is the first application of Ag_3BiI_6 in TM-SCs, and also includes a treatment study using 4tBP, biPY, CPDT-1, N719 and CuSCN.

2 Experimental

2.1 Precursor preparation

The Ag_3BiI_6 precursor was prepared by following the method of Turkevyvh et al.[10] Briefly, a mixed hot solvent (DMSO/DMF = 3 : 2, v/v, at 110 °C) was used to dissolve AgI/BiI_3 powder at a ratio of 3 : 1. 0.2 M 4tBP or biPY was dissolved in acetonitrile as nitrogen-containing pre-treatment. 0.5 mM N719 in acetonitrile/tert-butanol (1 : 1, v/v) and 0.05 mM CPDT-1 in chloroform/ethanol (3 : 7, v/v) were prepared as dye molecule precursors. The CuSCN precursor was prepared in diethyl sulphide (30 mg mL^{-1}) for post-treatment.

2.2 Device fabrication

FTO glass substrates (7 Ω sq^{-1}, Sigma-Aldrich) were prepared by etching the conductive side with Zn powder and 1 M HCl. Before use, the substrates were sequentially washed with detergent (Decon 90), DI water, acetone and isopropanol for 15 min each in a sonic bath, then placed in a UV/ozone chamber to remove the surface contamination residues. The c-TiO_2 precursor of 0.18 M titanium diisopropoxide bis(acetyl-acetonate) (75 wt% in isopropanol, Sigma-Aldrich) in 1-butanol was spin-coated on the FTO substrate at 4000 rpm for 30 s and then annealed at 450 °C for 30 min. The m-TiO_2 was subsequently screen-printed on top by using a TiO_2 slurry (Ti Nanoxide T/SP, Solaronix diluted with terpinol, 1 : 4 wt%), followed by annealing at 500 °C for 30 min on a programmable hotplate with a ramp rate of 10 °C min^{-1}. After cooling to room temperature, mesoporous ZrO_2 (m-ZrO_2) and carbon layers (obtained from National Laboratory for Optoelectronics, Wuhan) were deposited by screen-printing and annealed together at 400 °C for 30 min with the same temperature ramp rate. The device was filled with the absorber
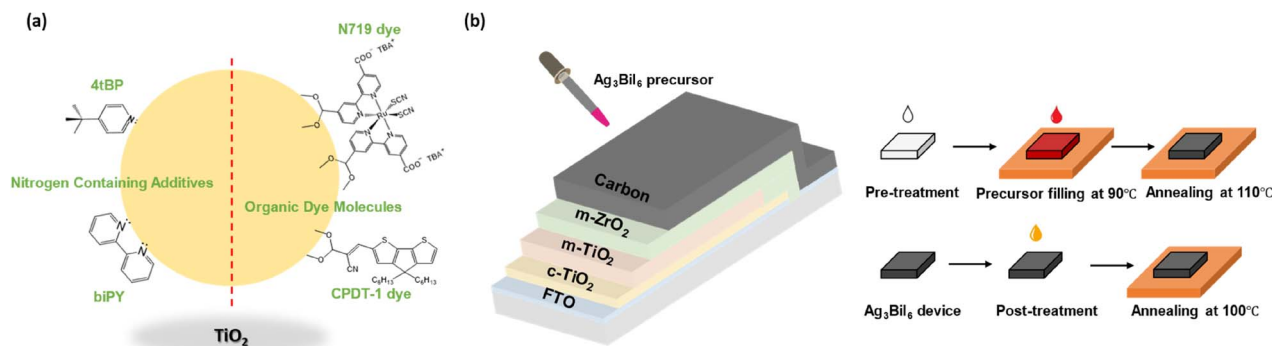

Fig. 1 (a) Schematic illustration of pre-treated attachment of 4tBP, biPY, N719 and CPDT-1 on TiO_2; (b) device configuration with the treatment procedure.

by dropwise addition of 6 μL Ag_3BiI_6 precursor on it, and then annealing was done at 110 °C for 3 h.

As illustrated in Fig. 1b, 4tBP, biPY, N719 or CPDT-1 precursors were drop-cast on the device and dried at room temperature for 30 min before introducing the Ag_3BiI_6 precursor; the CuSCN precursor was applied after the pores were thoroughly filled with Ag_3BiI_6 and annealing was done at 100 °C for 10 min.

2.3 Characterisation

The phase purity of thin films was identified using a Bruker D2 PHASER X-ray diffractometer (XRD) using Cu-Kα radiation with scattering angles (2θ) from 5–70°. All thin-film XRD samples were prepared on TiO_2 and ZrO_2 layers, where the carbon layer was omitted to avoid strong carbon peaks interfering with the desired XRD patterns. The top-view morphology images of mesoporous TiO_2/ZrO_2 filled with Ag_3BiI_6, cross-sectional device images and layered energy dispersive X-ray spectroscopy (EDS) images were recorded using a field emission scanning electron microscope (FE-SEM, Zeiss Sigma HD VP). The surface elemental analysis of Ag_3BiI_6 and CuSCN-treated Ag_3BiI_6 films was performed by X-ray photoelectron spectroscopy (XPS, Thermo Scientific VG Sigma Probe) using Al-Kα radiation. XPS samples were prepared on the bare glass to avoid any nonessential peaks from substrates. The diffuse reflectance spectroscopy of thin films was carried out on a Jasco V-670 UV/Vis/NIR spectrophotometer. Samples were prepared on the ZrO_2 substrate to facilitate pre-/post-treatments. The absorption spectra were measured and calculated according to the Kubelka–Munk theory within the wavelength range of 300–1000 nm. Photoluminescence (PL) quenching of pre-/post-treated Ag_3BiI_6 was recorded with a Fluoromax-3. Ag_3BiI_6 samples with pre-treatments were prepared on the TiO_2/ZrO_2

substrates; CuSCN-treated Ag_3BiI_6 samples were prepared on the ZrO_2 substrate to avoid any quenching effect of TiO_2. All PL samples were measured with an excitation wavelength of 500 nm at room temperature.

The current density–voltage (J–V) characteristics of the devices were measured using an AUTOLAB PGSTAT30 potentiostat. A solar simulator (Sciencetech-SF-150-B, AM1.5) was calibrated and used to provide 1000 W m^{-2} illumination. All devices were measured with varying potential bias from 0.02 V to −0.6 V at a scan rate of 100 mV s^{-1}. During the measurement, a metal mask with a 0.0314 cm^2 aperture area was used to prevent light scattering. Impedance spectroscopy was carried out on an AUTOLAB PGSTAT30 potentiostat in the frequency range from 100 mHZ to 1 MHz in the dark at 450 mV.

3 Results and discussion

3.1 Material characterisation

Thin-film X-ray diffraction measurements (XRD) were carried out to understand how treatments affect the formation of introduced Ag_3BiI_6 in mesoporous layers. The main diffraction peaks of the $TiO_2/ZrO_2/Ag_3BiI_6$ sample correspond to highly crystalline phases with $R\bar{3}m$ symmetry for the Ag_3BiI_6 pattern concerning both positions and intensities, with reflections corresponding to the (003), (010), (102), (104), (105), (110), (108) and (204) planes at 12.8°, 24.1°, 25.2°, 29.4°, 32.2°, 41.6°, 42.4° and 51.8°, respectively (Fig. 2a).[16] Consistent with previous studies, the three distinct diffraction peaks at 22.3°, 39.2° and 46.3° correspond to the impurity of AgI, originating from the silver-rich precursor that is required to prepare Ag_3BiI_6.[27] Beyond this, no other impurity was identified. Fig. 2b compares the results of Ag_3BiI_6 with different pre-treatments on the mesoporous surface. Consistent patterns suggest that the pre-
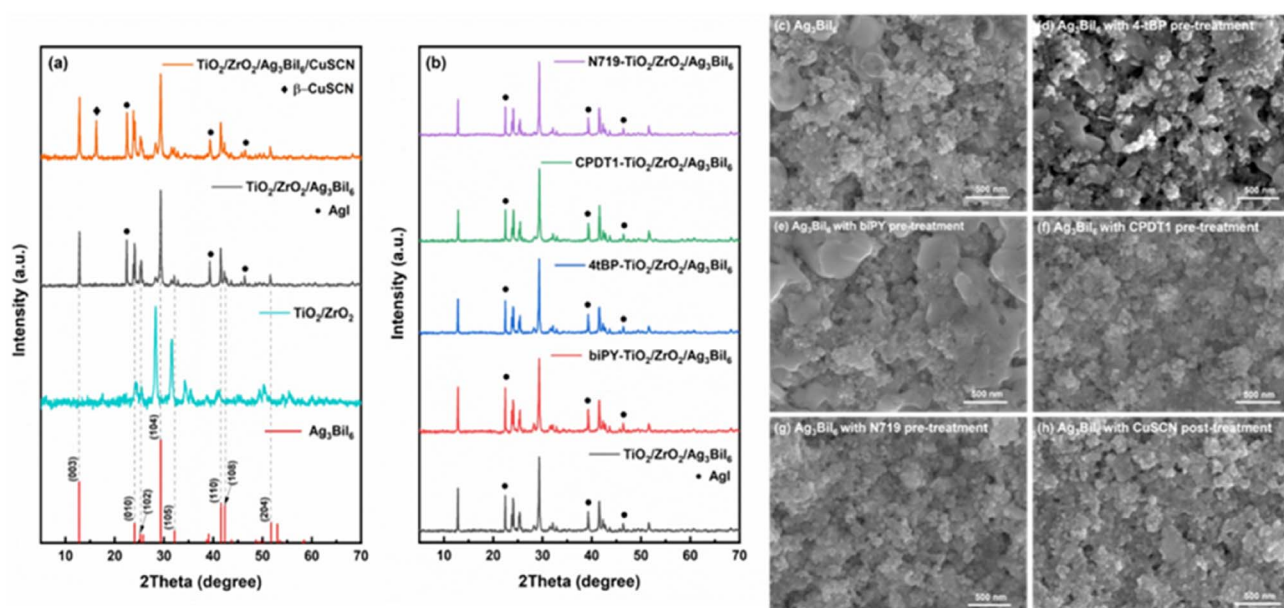

Fig. 2 (a) XRD patterns of the TiO_2/ZrO_2 substrate with Ag_3BiI_6 and Ag_3BiI_6 with CuSCN-treatment; (b) XRD patterns of Ag_3BiI_6 with pre-treatments. Top-view SEM images of (c) Ag_3BiI_6 with (d) 4tBP, (e) biPY, (f) CPDT-1 and (g) N719 pre-treatment; and (h) CuSCN post-treatment.
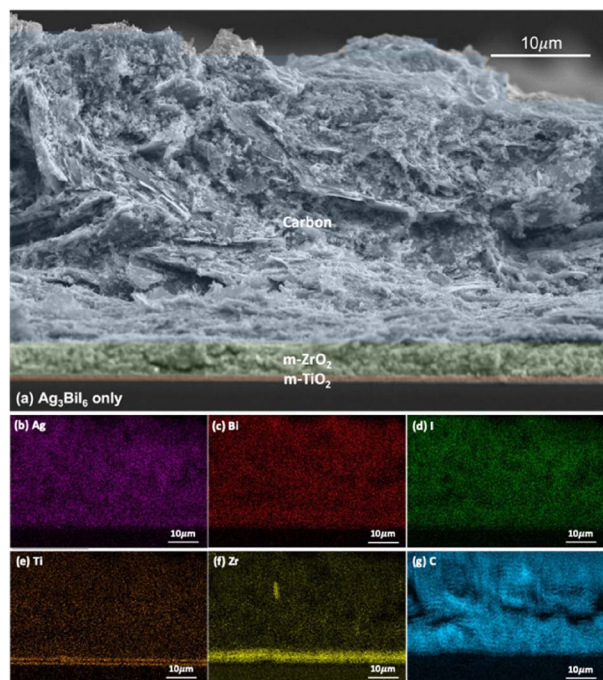
Fig. 3 (a) Cross-sectional SEM image of the device filled with only Ag_3BiI_6 and EDS mapsof (b) Ag, (c) Bi, (d) I, (e) Ti, (f) Zr, and (g) C.

treatments barely affect the formation or morphology of Ag_3BiI_6 on the substrates. Fig. 2a also shows the XRD result of CuSCN treated samples, where a strong peak at 16.6° indicates the existence of β-CuSCN.[28] Although a previous study showed that spin-coating CuSCN on Ag_3BiI_6 washed away the underlying Ag_3BiI_6 film, in this case, by drop-casting CuSCN on the device, Ag_3BiI_6 is firmly retained within the mesoporous scaffold instead of being removed.[14] Interestingly, Ag_3BiI_6 was observed first to dissolve in the CuSCN precursor and then slowly crystallise when the substrates were heated up, as the colour changed from black to dark orange and then turned back to black (Fig. S1†). After annealing, the Ag_3BiI_6 recrystallised and mixed with CuSCN.

Top-view SEM images were recorded to reveal the morphology of Ag_3BiI_6 crystallites with different treatment procedures. Fig. 2c shows the well-defined ZrO_2 particle boundaries (~30 nm) filled with Ag_3BiI_6 and slightly covered with the Ag_3BiI_6 crust. A similar surface morphology was observed with 4tBP and biPY treatments (Fig. 2d and e), indicating that the pore filling process is unaffected by the N-donor molecule treatment. A more compact mesoporous film was obtained after the mesoporous layer was treated with CPDT-1 and N719, as shown in Fig. 2f and g. It seems that the wettability of the mesoporous layers is better modified by the carboxyl-binding dye molecules than the Ti–N bonds of N-donor molecules, resulting in better Ag_3BiI_6 precursor infusion. Fig. 2h shows that the Ag_3BiI_6 crust disappears with the CuSCN treatment. The most likely reason for such an observation is that Ag_3BiI_6 re-dissolves in the CuSCN precursor solution and penetrates deeper into the mesoporous layer. However, these findings may be affected by the absence of the carbon layer, and

it is essential to bear in mind that these images only suggest an approximation of the actual pore-filling process in the full device.

Cross-sectional SEM images with energy dispersive X-ray spectroscopy (EDS) mapping were recorded to comprehend the element distribution of the Ag_3BiI_6 containing full devices. Fig. 3 illustrates the component element (Ag/Bi/I) distribution reaching the very bottom TiO_2 layer, indicating thorough penetration of Ag_3BiI_6. A detailed investigation of how Ag_3BiI_6 penetrates with different treatments is provided in Fig. S2.† As indicated from top-view SEM images, an even distribution of Ag_3BiI_6 was observed with pre-treatments, suggesting unchanged pore filling. However, with CuSCN post-treatment, AgI is found to accumulate in the upper carbon layer, providing evidence of the re-dissolving process and constricting Ag_3BiI_6 to a thinner layer. The cross-sectional SEM images and selected EDS maps (Ag/Bi/Zr/Cu) are shown in Fig. 4, indicating that CuSCN (Fig. 4e) is ideally placed on the top of the absorber (mainly staying in the carbon layer and upper ZrO_2 layer) to play a role in the hole extraction.

Diffuse reflectance spectroscopy provides surface optical information on solid-state materials. The absorption spectra were therefore employed to investigate the effect of pre-/post-treatment on the optical properties of Ag_3BiI_6. The absorption results following different pre-treatments are identical in the visible region (Fig. S3a†), and a direct bandgap of 1.79 eV was obtained (inset in Fig. S3a†). Compared with results obtained from previous studies, the smaller experimental value here is possibly due to the increased thickness of Ag_3BiI_6 (~3 μm), which is thicker than the Ag_3BiI_6 film deposited by spin-coating.[29] In this case, the thicker film particularly reduces the light transmittance and shifts the corresponding absorption edge to a longer wavelength, resulting in a smaller measured bandgap. However, with CuSCN treatment, a slight loss in absorption is observed in the spectrum (Fig. S3b†). This discrepancy could be attributed to less material in the central measuring area, caused by spreading of the CuSCN precursor
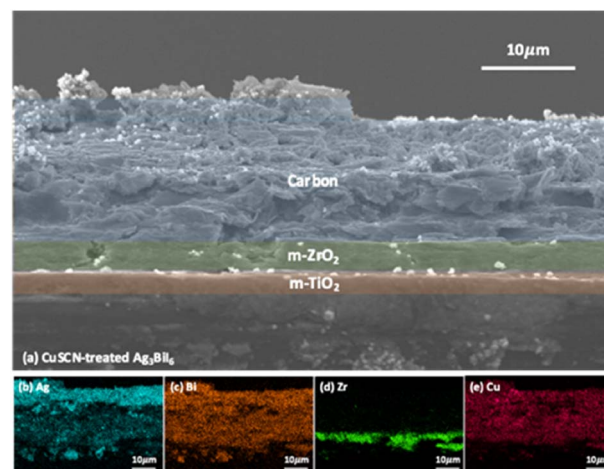

Fig. 4 (a) Cross-sectional SEM image of CuSCN post-treated Ag_3BiI_6 device and EDS maps of (b) Ag, (c) Bi, (d) Zr, and (e) Cu.

solution that pushes part of Ag_3BiI_6 to the edge. Despite this, the absorption covers most of the visible region.

The interaction between Ag_3BiI_6 and CuSCN was investigated by X-ray photoelectron spectroscopy (XPS). The survey spectra (Fig. S4†) confirm the major elements (*e.g.*, Ag, Bi, and I) in Ag_3BiI_6 films, and a weak peak at 932.4 eV related to Cu 2p was detected in the CuSCN treated film. High-resolution spectra (Fig. 5a) show that Ag 3d5/2, Bi 4d5/2 and I 3d5/2 peaks appear at the same position with a negligible shift, indicating a consistent chemical state of Ag_3BiI_6. The Ag 3d5/2 peak at the binding energy of 368.20/368.19 eV includes two weak peaks at 368.97/368.88 eV (green) and 367.19/367.16 eV (violet). The peaks at 368.97 eV and 368.88 eV are attributed to metallic Ag, while peaks at 367.19 eV and 367.16 eV correspond to AgI.[30] This result confirms the existence of excess Ag or Ag^+. Fig. 5b shows the sole peak of Bi 4d5/2 at the binding energy of 442.18/442.26 eV. Although Bi 4f is the first choice for element analysis in XPS, Bi 4d, which gives the same information, is used here because the binding energy of Bi 4f and S 2p are close, at ~164 eV and ~167.5 eV, respectively, complicating the deconvolution. The I 3d5/2 peak at the binding energy position of 619.31/619.38 eV is further deconvoluted at 620.83/620.96 eV (violet) and 617.92/617.97 eV (green), which are likely related to
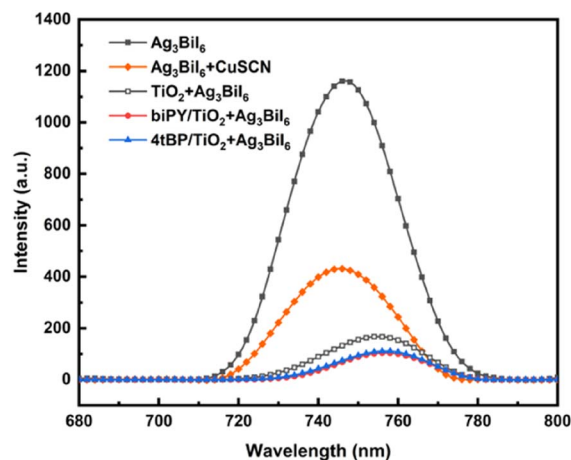

Fig. 6 Steady-state PL quenching spectra of Ag_3BiI_6 with different treatments on the mesoporous film.

BiI_3 and AgI, respectively (Fig. 5c).[31] The peak of the Cu 2p3/2 binding energy was observed at 932.39 eV, as shown in Fig. 5d. The central peak at the binding energy position of 931.92/932.39 eV (blue) is attributed to Cu^+ with SCN^- (in tetrahedral coordination), while the weaker ones at 930.18/929.14 eV (green) are likely associated with Cu_2O impurities.[32,33] The lowest binding energy peak at 928.65/926.88 eV (violet) is possibly related to Cu metal.[34] Further analysis of the data revealed that the I 3p1/2 peak at 930.61 eV overlapped with the deconvoluted peaks of Cu 2p3/2.

Photoluminescence (PL) spectroscopy was carried out to examine the electron and hole donating ability of Ag_3BiI_6 at TiO_2 and CuSCN interfaces. Fig. 6 presents the results obtained from PL spectroscopy. A change in Ag_3BiI_6 emission was observed when it was deposited on TiO_2 substrates and a noticeable quenching effect was found with N-donor treatment, explaining why greater V_{oc} was obtained in devices with pre-treatment (*vide infra*). On the other hand, a significant emission suppression was observed in the mixture of Ag_3BiI_6/CuSCN, facilitating hole transfer. These results suggest that the N-donor and CuSCN help to extract charge carriers more efficiently within mesoporous layers, suggesting that performance improvement in TM-SCs should occur.

3.2 Device characterisation

Ag_3BiI_6 TM-SCs were fabricated to study the device performance with different treatments. Although perovskites have been widely applied in TM-SCs, the reproducibility of device fabrication remains challenging due to variation in the spontaneous precursor pore filling, affected by solution viscosity, annealing temperature or ventilation conditions. Given the novelty of our devices that use the Ag_3BiI_6 absorber, and the general difficulties of reproducibility, we focus on the champion devices for discussion, although some consideration of average results is also given where appropriate. *J–V* curves of the as-prepared devices are shown in Fig. 7, and the corresponding device parameters are summarised in Table 1.
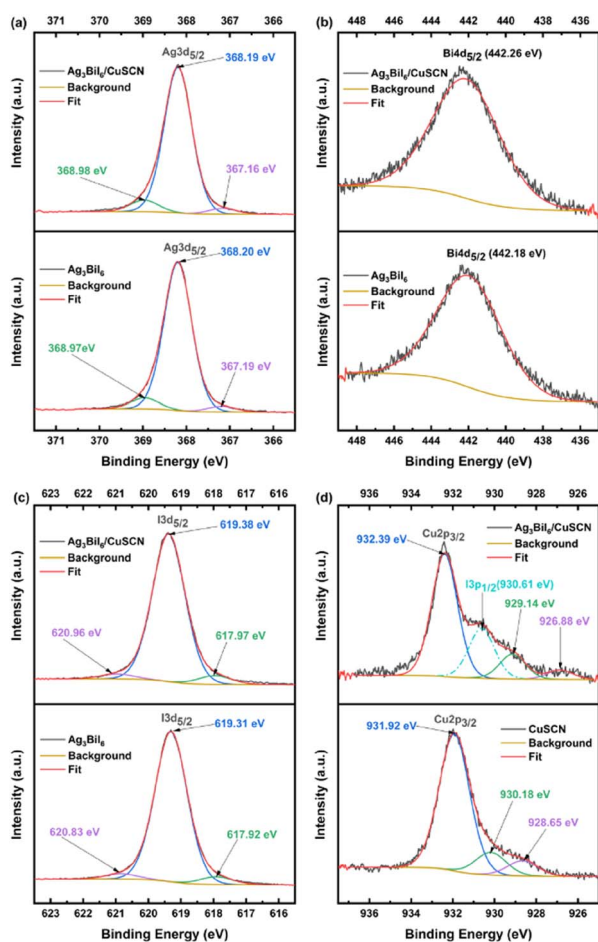

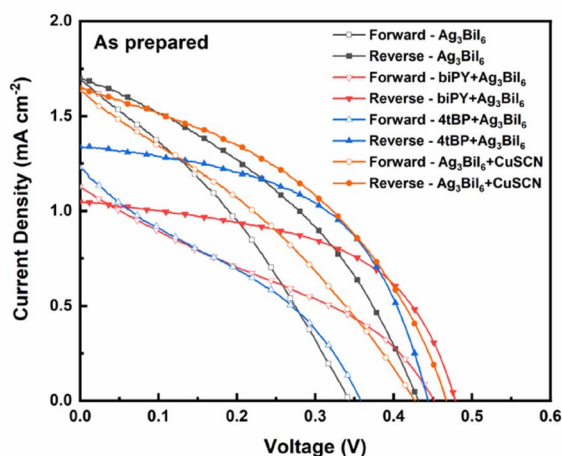Fig. 5 High-resolution XPS spectra of (a) Ag 3d5/2, (b) Bi 4d5/2, (c) I 3d5/2 and (d) Cu 2p3/2.

Fig. 7 J–V curves of as-prepared Ag_3BiI_6 TM-SC devices with biPY, 4tBP and CuSCN treatments.

The Ag_3BiI_6 devices showed photo-response with hysteresis behaviour under illumination, indicating the existence of defects and/or vacancy-mediated ion migration in Ag_3BiI_6.[35,36] It is apparent from Fig. 7 and Table 1 that the devices with 4tBP and biPY pre-treatments yield an improved V_{oc}. With biPY, V_{oc} was improved from 0.42 V to 0.48 V. These results agree with previous studies on DSSCs, in which the conduction band of TiO_2 was negatively shifted to improve V_{oc}.[35] However, applying the N-donor molecule, such as 4tPB and biPY, may have introduced a series resistance at the TiO_2 interface, leading to low J_{sc}.[37] Therefore, the overall as-prepared performance of N-donor treated devices remains largely unchanged.

When comparing the results of dye molecule treated devices, the performance is poor due to low J_{sc} (Fig. S5 and Table S1†). The energy level alignment mismatch may hinder electron–hole extraction because the lowest occupied molecular orbital (LUMO) of CPDT-1 (−2.8 eV) and N719 (−3.6 eV) is higher than

or at the same position compared to the reported conduction band of Ag_3BiI_6 (−3.6 eV), creating a barrier for electron injection (Fig. S6†).[15,23,38,39] Therefore, the electron from Ag_3BiI_6 could be hampered, causing a high recombination rate within Ag_3BiI_6.

CuSCN devices demonstrated an increased V_{oc} with minor J_{sc} loss, which is likely attributed to better hole extraction. As N-donor molecule pre-treatment exhibited better performance than dyes, an attempt has been made at joint-treatment using biPY and 4tBP with CuSCN. Surprisingly, the joint-treatment devices demonstrated serious hysteresis behaviour and less efficient performance, than the devices with only CuSCN (Fig. S5†).

The calculated hysteresis index, HI, is compared to evaluate the hysteresis level (listed in Table S1†). HI can be calculated using the following equation:

$$HI = \frac{PCE_{reverse} - PCE_{forward}}{PCE_{reverse}}$$
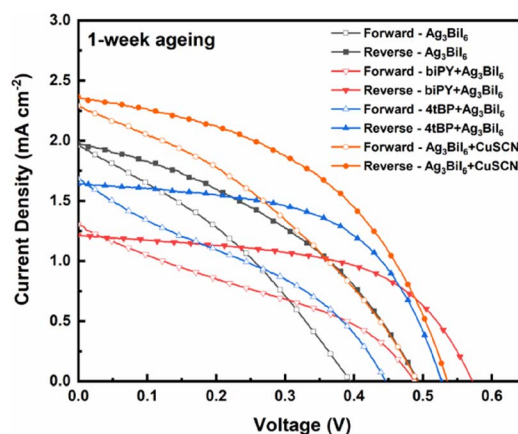

Fig. 8 J–V curve of 1 week aged Ag_3BiI_6 TM-SC devices with biPY, 4tBP and CuSCN treatments.

Table 1 J–V characteristic parameters of as-prepared Ag_3BiI_6 TM-SCs with biPY, 4tBP and CuSCN treatments[a]

Device	Ageing	Scan	J_{sc} [mA cm^{-2}]	V_{oc} [V]	FF	PCE (%)
Ag_3BiI_6 only	As-prepared	Forward	1.69 (1.48 ± 0.28)	0.34 (0.34 ± 0.02)	0.33 (0.31 ± 0.02)	0.19 (0.16 ± 0.04)
		Reverse	1.70 (1.50 ± 0.28)	0.43 (0.42 ± 0.02)	0.39 (0.36 ± 0.03)	0.28 (0.24 ± 0.06)
biPY + Ag_3BiI_6	As-prepared	Forward	1.12 (1.06 ± 0.16)	0.45 (0.44 ± 0.02)	0.32 (0.31 ± 0.04)	0.16 (0.14 ± 0.04)
		Reverse	1.05 (0.99 ± 0.12)	0.48 (0.48 ± 0.01)	0.53 (0.49 ± 0.04)	0.27 (0.23 ± 0.02)
4tBP + Ag_3BiI_6	As-prepared	Forward	1.22 (1.17 ± 0.20)	0.36 (0.36 ± 0.04)	0.33 (0.32 ± 0.04)	0.14 (0.13 ± 0.03)
		Reverse	1.34 (1.23 ± 0.28)	0.44 (0.43 ± 0.01)	0.53 (0.46 ± 0.07)	0.32 (0.24 ± 0.05)
Ag_3BiI_6 + CuSCN	As-prepared	Forward	1.63 (1.47 ± 0.21)	0.43 (0.40 ± 0.02)	0.32 (0.34 ± 0.05)	0.22 (0.20 ± 0.04)
		Reverse	1.65 (1.46 ± 0.21)	0.47 (0.46 ± 0.01)	0.42 (0.43 ± 0.04)	0.33 (0.29 ± 0.05)
Ag_3BiI_6 only	1 week aged	Forward	1.95 (1.75 ± 0.40)	0.39 (0.37 ± 0.05)	0.34 (0.32 ± 0.03)	0.26 (0.21 ± 0.08)
		Reverse	1.97 (1.79 ± 0.36)	0.49 (0.49 ± 0.02)	0.39 (0.36 ± 0.05)	0.38 (0.32 ± 0.10)
biPY + Ag_3BiI_6	1 week aged	Forward	1.30 (1.12 ± 0.12)	0.49 (0.47 ± 0.02)	0.33 (0.33 ± 0.01)	0.21 (0.17 ± 0.03)
		Reverse	1.21 (1.07 ± 0.10)	0.57 (0.57 ± 0.01)	0.56 (0.50 ± 0.06)	0.39 (0.30 ± 0.05)
4tBP + Ag_3BiI_6	1 week aged	Forward	1.68 (1.33 ± 0.27)	0.44 (0.42 ± 0.03)	0.34 (0.34 ± 0.03)	0.25 (0.19 ± 0.04)
		Reverse	1.64 (1.33 ± 0.28)	0.52 (0.51 ± 0.01)	0.57 (0.46 ± 0.08)	0.49 (0.31 ± 0.11)
Ag_3BiI_6 + CuSCN	1 week aged	Forward	2.28 (2.16 ± 0.53)	0.49 (0.45 ± 0.03)	0.36 (0.37 ± 0.04)	0.40 (0.35 ± 0.07)
		Reverse	2.35 (2.17 ± 0.62)	0.53 (0.51 ± 0.02)	0.47 (0.48 ± 0.05)	0.60 (0.52 ± 0.09)

[a] The average results in brackets were calculated from 5 individual devices for each type.
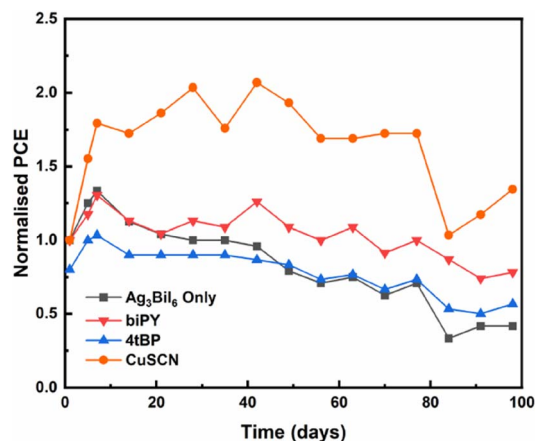
Fig. 9 Dark storage PCE stability (reverse scan) of Ag_3BiI_6 devices with biPY, 4tBP and CuSCN treatments in the ambient atmosphere.

Interestingly, HI is smaller in those devices without any pre-treatment (with/without CuSCN post-treatment). With the presence of CuSCN, HI is slightly smaller than that of Ag_3BiI_6 only devices, indicating efficient charge extraction. Although CuSCN may re-dissolve Ag_3BiI_6, remaining Ag^+ in the meso-porous layer could potentially create more defects, obstructing the charge separation by charge accumulation at interfaces.

Stability was evaluated for all fabricated solar cells, following the ambient dark storage protocol of the International Summit on OPV stability (ISOS) protocol—ISOS-D-1.[40] The performance of all devices was recorded for 99 days, and consistent efficiency with the initial devices was found. Fig. 8 presents the one-week device performance regarding the ageing effect, and the corresponding device parameters are summarised in Table 1.

Fig. 8 and Table 1 show that the performance of all devices increased after one-week ageing (more details in Fig. S7 and Table S2†). Slow solvent evaporation and crystallisation process are likely to be the underlying factors to improve V_{oc} and J_{sc}. It is worth noting that the efficiency of the champion CuSCN treated device doubled from 0.33% (day 1) to 0.60% (day 7) and peaked at 0.74% on day 28 (Table S2†). Besides, the HI of the CuSCN-treated devices reduced after 14 days, from 0.30 to 0.25. When comparing the dark storage stability parameters (Fig. 9 and S8†), the increased PCE is mainly due to J_{sc} improvement where V_{oc} and FF results maintain a stable level. The distinct performance decay after day 80 is mainly caused by fatigue in the devices due to repeated impedance measurements. Nevertheless, the overall results indicate satisfactory ageing stability, also suggesting that better device efficiency could be obtained by improving the initial performance.

Electrochemical impedance spectroscopy (EIS) measurements were conducted to study the charge transport and transfer processes in the devices. A previous study on perovskite TM-SCs has reported two major features of EIS: the intermediate-frequency arc and the low-frequency arc, associated with the bulk recombination of perovskite and the interface phenomena, respectively.[41] Fig. 10a and b and S9† show the Nyquist and Bode plots of devices measured at 450 mV in the dark. In this case, three arcs are observed in EIS measurement:

(i) The first arc in the high-frequency region (10^5–10^6 Hz) remains almost unchanged with varying bias, which is attributed to the carbon/FTO interface on the counter electrode side for hole extraction;

(ii) The second arc in the intermediate frequency region (10^1–10^5 Hz) is related to the bulk Ag_3BiI_6 recombination (R_{rec}),
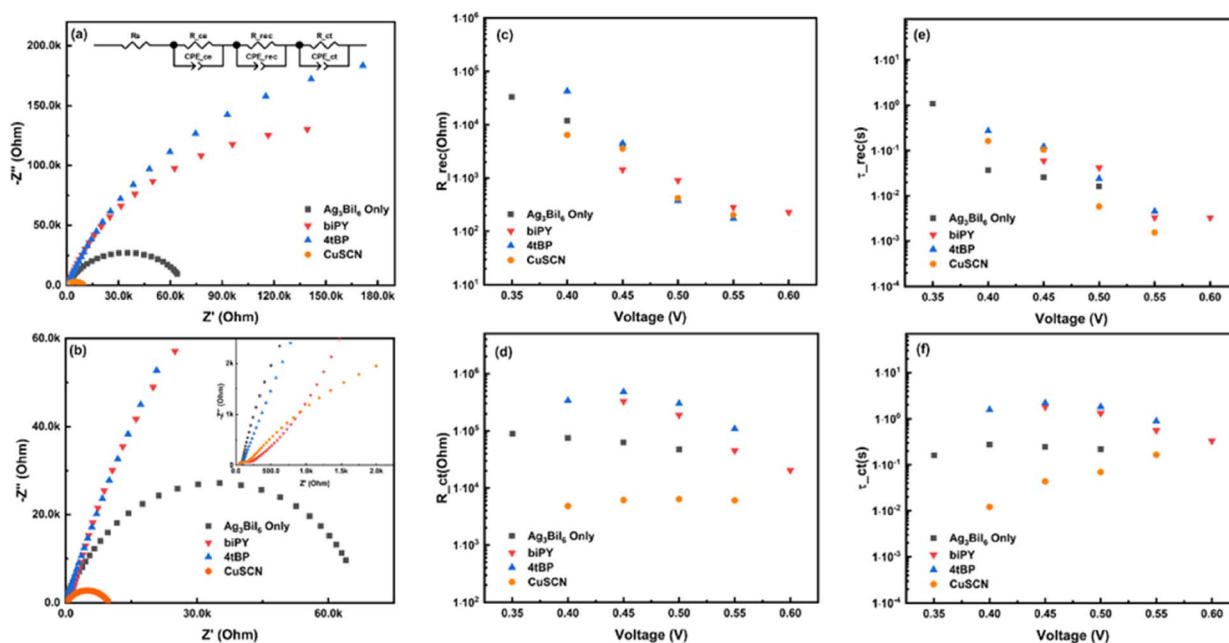

Fig. 10 (a) and (b) Nyquist plots of Ag_3BiI_6 TM-SCs only and with biPY, 4tBP and CuSCN treatments at 450 mV in the dark; values of extracted resistance of (c) R_{rec} and (d) R_{ct}; calculated lifetime of (e) τ_{rec} and (f) τ_{ct}.

Table 2 Summary of efficiency of Ag_3BiI_6 based solar cells[a]

Device structure	J_{sc} [mA cm^{-2}]	V_{oc} [V]	FF	PCE (%)	Method	Description
FTO/c-TiO$_2$/m-TiO$_2$/Ag$_3$BiI$_6$/P3HT/Au	5.12	0.58	0.61	1.80	Spin-coating (with an anti-solvent)	This study proposed a triple-ion-migration-induced degradation mechanism that mainly occurred in Ag-rich pnictohalides[36]
ITO/NiO$_x$/Ag$_3$BiI$_6$/PCBM + C60/Au	1.73	0.82	0.76	1.08	Spin-coating in a glovebox	This study reported an inverted (p-i-n) solar cell using dynamic casting in combination with a ramped annealing procedure[42]
FTO/c-TiO$_2$/m-TiO$_2$/A Ag$_3$BiI$_6$/PTAA/Au	10.70	0.63	0.64	4.30	Spin-coating	AgI was first reported to be dissolved in hot DMSO with BiI$_3$, which makes pnictohalide solution-process available[10]
FTO/c-TiO$_2$/m- TiO$_2$/Ag$_3$BiI$_6$/spiro-OMeTAD/Au	2.36	0.65	0.70	1.08	Spin-coating in a glovebox	This study compared MA$_3$Bi$_2$I$_9$, Ag$_3$BiI$_6$ and Cu$_3$BiI$_6$ in both
FTO/NiO/Ag$_3$BiI$_6$/PCBM/BCP/Ag	1.29	0.41	0.59	0.32	Spin-coating in a glovebox	normal (n-i-p) and inverted (p-i-n) configurations[43]
FTO/c-TiO$_2$/m-TiO$_2$/Ag$_3$BiI$_6$/PTAA/Au	11.20	0.61	0.65	4.38	Spin-coating in a glovebox	This study partially replaced I$^-$ with S^{2-} in Ag$_3$BiI$_6$ to adjust the optical band gap of pnictohalides. Ag$_3$BiI$_{5.92}$S$_{0.04}$ achieved 5.44% efficiency[15]
FTO/c-TiO$_2$/m-TiO$_2$/Ag$_3$BiI$_6$/spiro-OMeTAD/Au	1.00	0.35	0.35	0.12	Spin-coating	This study illustrated the sulphur incorporation effect of multi-walled carbon nanotubes and reduced graphene oxide on silver pnictohalides[44]
FTO/c-TiO$_2$/m-TiO$_2$/m-ZrO$_2$/Carbon (introduced Ag$_3$BiI$_6$)	2.78	0.56	0.48	0.74	Screen-printing and drop-casting in the ambient atmosphere	Our study first introduced Ag$_3$BiI$_6$ in triple-mesoporous solar cells with additional treatment procedures. With CuSCN post-treatment, the champion device efficiency improved to 0.74% after aging. (This work)

[a] BCP: bathocuproine.

although it is barely observed in the Nyquist plot due to significant overlap;

(iii) The third arc in the low-frequency region (10^{-1}–10^1 Hz) is different for each device, which is likely to be associated with the Ag$_3$BiI$_6$/TiO$_2$ interface. Three R–C elements were applied to simulate the equivalent circuit in this case (Fig. 10a inset). The series resistance (R_s) represents the general transport resistance of the FTO substrate and external circuit. In the Nyquist plot, the CuSCN treated devices exhibit a minor feature, while biPY and 4tBP pre-treatment devices show a much more significant feature. This amplified feature has been highlighted in the perovskite.

A strong relationship of the arc feature in TM-SCs is reported to be related to perovskite thickness.[41] As discussed in the previous section (cross-sessional EDS layered images), the CuSCN-treated device exhibits a thinner layer when compared to other devices due to a re-dissolving process, while the enlarged feature of biPY and 4tBP is possibly due to increased thickness, although it is difficult to tell from the EDS results.

Fig. 10c–f show the extracted results of charge transfer resistance (R_{rec} and R_{ct}), and calculated lifetime (τ_{rec} and τ_{ct}) as a function of the applied potential for the solar cells. R_{rec} and the corresponding lifetime, $\tau_{rec} = R_{rec} \times C_{rec}$, gave similar values in all devices regardless of the treatment procedure, indicating the consistent bulk recombination resistance of Ag$_3$BiI$_6$ (Fig. 10c and e). However, we observed a slight difference in the results of R_{ct} and τ_{ct} ($\tau_{ct} = R_{ct} \times C_{ct}$), as shown in Fig. 10f and d, respectively: N-donor molecules lead to higher charge transfer resistance and a longer charge lifetime in the devices; while CuSCN treated devices exhibit smaller resistance and a shorter electron lifetime than the non-treated devices, which may due to the physical mixture of Ag$_3$BiI$_6$ and CuSCN. It is worth noting that R_{rec} mainly appears in the frequency range of 10^1–10^5 Hz, implying a higher frequency process than the charge extraction to TiO$_2$, which may explain the low V_{oc} value obtained from the devices. The corresponding capacitances (C_{rec} and C_{ct}) are shown in Fig. S10.† However, it is difficult to explain the corresponding C_{rec} trend, which might be related to the fitting errors due to the severe overlap of the semicircles in the intermediate-low frequency region.

4 Conclusions

In summary, this study demonstrated Ag$_3$BiI$_6$ as an absorber in TM-SCs and examined the role of pre-treatment (biPY, 4tBP, N719 and CPDT-1) and post-treatment (CuSCN) in device

performance. The cross-sectional SEM and EDS layered images have shown the thorough penetration of Ag_3BiI_6 in all devices. Although we observed a re-dissolving process upon CuSCN treatment, which led to thinner Ag_3BiI_6, the Ag_3BiI_6 component is only slightly affected by this re-dissolving process, as shown by consistent results obtained from XRD, UV/vis and XPS. Also, the steady-state PL intensity revealed the enhanced hole extraction with CuSCN treatment. Based on this characterisation of Ag_3BiI_6 in mesoporous layers, we fabricated Ag_3BiI_6 TM-SCs, demonstrating a best as-prepared PCE of 0.33%. Pretreatment made no significant difference to device performance. However, CuSCN provides superior charge collection in the device, which boosted the device PCE to 0.74% after ageing. All devices exhibited satisfactory dark storage stability for up to 80 days with no encapsulation. Table 2 compares the PCE of current Ag_3BiI_6 TM-SCs with that of conventional Ag_3BiI_6 devices reported previously. These results suggest the feasibility of Ag_3BiI_6 in low-cost and carbon-based solar cells and the role of additional device treatment in promoting PCE, extending our understanding of Bi-based materials in TM-SCs. Although this study has demonstrated a promising pathway for developing Bi-based TM-SCs, performance is limited by hysteresis and reproducibility issues. Previous Ag_2BiI_5 device studies noted that a thicker absorbing layer leads to higher carrier recombination, suggesting that future work could focus on modifying the thickness of the ZrO_2 layer so as to facilitate charge transfer.[45,46] Further work could also assess the TiO_2/Ag_3BiI_6 surface engineering on the device, the Ag_3BiI_6 precursor or the annealing process to perform better pore filling and reduce non-radiative recombination. Furthermore, CuSCN could be replaced by other Cu-based inorganic HTMs or NiO_x to avoid the re-crystallising process. These additional engineering steps may enable us to develop higher efficiency and better reproducibility in TM-SCs.

Conflicts of interest

There are no conflicts to declare.

Acknowledgements

Notes and references

1 A. Mei, X. Li, L. Liu, Z. Ku, T. Liu, Y. Rong, M. Xu, M. Hu, J. Chen, Y. Yang, et al., Science, 2014, 345, 295–298.
2 Y. Rong, Y. Hu, A. Mei, H. Tan, M. I. Saidaminov, S. I. Seok, M. D. McGehee, E. H. Sargent and H. Han, Science, 2018, 361, eaat8235.
3 K. Yang, S. Liu, J. Du, W. Zhang, Q. Huang, W. Zhang, W. Hu, Y. Hu, Y. Rong, A. Mei, et al., Sol. RRL, 2021, 5, 2000825.
4 Y. Hu, Z. Zhang, A. Mei, Y. Jiang, X. Hou, Q. Wang, K. Du, Y. Rong, Y. Zhou, G. Xu, et al., Adv. Mater., 2018, 30, 1705786.
5 T. Wu, Y. Wang, X. Li, Y. Wu, X. Meng, D. Cui, X. Yang and L. Han, Adv. Energy Mater., 2019, 9, 1803766.
6 L. Xu, Y. Li, J. Shi, N. Robertson, W. Wu, Q. Meng and H. Tian, Sol. RRL, 2020, 4, 2000042.
7 Y. Guan, A. Mei, Y. Rong, M. Duan, X. Hou, Y. Hu and H. Han, Org. Electron., 2018, 62, 653–659.
8 I. Zimmermann, P. Gratia, D. Martineau, G. Grancini, J.-N. Audinot, T. Wirtz and M. K. Nazeeruddin, J. Mater. Chem. A, 2019, 7, 8073–8077.
9 Y. Kim, Z. Yang, A. Jain, O. Voznyy, G.-H. Kim, M. Liu, L. N. Quan, F. P. García de Arquer, R. Comin, J. Z. Fan, et al., Angew. Chem., Int. Ed., 2016, 55, 9586–9590.
10 I. Turkevych, S. Kazaoui, E. Ito, T. Urano, K. Yamada, H. Tomiyasu, H. Yamagishi, M. Kondo and S. Aramaki, ChemSusChem, 2017, 10, 3754–3759.
11 A. Chakraborty, N. Pai, J. Zhao, B. R. Tuttle, A. N. Simonov and V. Pecunia, Adv. Funct. Mater., 2022, 32, 2203300.
12 H. Zhu, M. Pan, M. B. Johansson and E. M. Johansson, ChemSusChem, 2017, 10, 2592–2596.
13 B. Ghosh, B. Wu, X. Guo, P. C. Harikesh, R. A. John, T. Baikie, A. T. Wee, C. Guet, T. C. Sum, S. Mhaisalkar, et al., Adv. Energy Mater., 2018, 8, 1802051.
14 M. Khazaee, K. Sardashti, C.-C. Chung, J.-P. Sun, H. Zhou, E. Bergmann, W. A. Dunlap-Shohl, Q. Han, I. G. Hill, J. L. Jones, et al., J. Mater. Chem. A, 2019, 7, 2095–2105.
15 N. Pai, J. Lu, T. R. Gengenbach, A. Seeber, A. S. Chesman, L. Jiang, D. C. Senevirathna, P. C. Andrews, U. Bach, Y.-B. Cheng, et al., Adv. Energy Mater., 2019, 9, 1803396.
16 T. Oldag, T. Aussieker, H.-L. Keller, C. Preitschaft and A. Pfitzner, Z. Anorg. Allg. Chem., 2005, 631, 677–682.
17 L. F. Mashadieva, Z. S. Aliev, A. V. Shevelkov and M. B. Babanly, J. Alloys Compd., 2013, 551, 512–520.
18 T. Li, Y. Hu, C. A. Morrison, W. Wu, H. Han and N. Robertson, Sustainable Energy Fuels, 2017, 1, 308–316.
19 T. Li, Q. Wang, G. S. Nichol, C. A. Morrison, H. Han, Y. Hu and N. Robertson, Dalton Trans., 2018, 47, 7050–7058.
20 P. T. Nguyen, P. E. Hansen and T. Lund, Sol. Energy, 2013, 88, 23–30.
21 P. T. Nguyen, T. A. P. Phan, N. H. T. Ngo, T. Van Huynh and T. Lund, Solid State Ionics, 2018, 314, 98–102.
22 F. Tan, M. I. Saidaminov, H. Tan, J. Z. Fan, Y. Wang, S. Yue, X. Wang, Z. Shen, S. Li, J. Kim, et al., Adv. Funct. Mater., 2020, 30, 2005155.
23 Y. Hu, A. Abate, Y. Cao, A. Ivaturi, S. M. Zakeeruddin, M. Gratzel and N. Robertson, J. Phys. Chem. C, 2016, 120, 15027–15034.
24 X. Lin, J. Lu, S. R. Raga, D. P. McMeekin, Q. Ou, A. D. Scully, B. Tan, A. S. Chesman, S. Deng, B. Zhao, et al., Adv. Energy Mater., 2021, 11, 2100053.
25 N. Wijeyasinghe, A. Regoutz, F. Eisner, T. Du, L. Tsetseris, Y. H. Lin, H. Faber, P. Pattanasattayavong, J. Li, F. Yan, et al., Adv. Funct. Mater., 2017, 27, 1701818.

26 N. Arora, M. I. Dar, A. Hinderhofer, N. Pellet, F. Schreiber, S. M. Zakeeruddin and M. Grätzel, *Science*, 2017, **358**, 768–771.

27 S. Hull and D. Keen, *Phys. Rev. B: Condens. Matter Mater. Phys.*, 1999, **59**, 750.

28 D. Smith and V. Saunders, *Acta Crystallogr., Sect. B: Struct. Crystallogr. Cryst. Chem.*, 1982, **38**, 907–909.

29 A. Crovetto, A. Hajijafarassar, O. Hansen, B. Seger, I. Chorkendorff and P. C. Vesborg, *Chem. Mater.*, 2020, **32**, 3385–3395.

30 S. Ning, H. Lin, Y. Tong, X. Zhang, Q. Lin, Y. Zhang, J. Long and X. Wang, *Appl. Catal., B*, 2017, **204**, 1–10.

31 S. Gaarenstroom and N. Winograd, *J. Chem. Phys.*, 1977, **67**, 3500–3506.

32 J. S. McCloy, C. Leslie, T. Kaspar, W. Jiang and R. K. Bordia, *J. Appl. Phys.*, 2012, **111**, 07E149.

33 M. Monte, G. Munuera, D. Costa, J. C. Conesa and A. Martínez-Arias, *Phys. Chem. Chem. Phys.*, 2015, **17**, 29995–30004.

34 D.-H. Nam, B. J. Taitt and K.-S. Choi, *ACS Catal.*, 2018, **8**, 1197–1206.

35 G. Tumen-Ulzii, T. Matsushima, D. Klotz, M. R. Leyden, P. Wang, C. Qin, J.-W. Lee, S.-J. Lee, Y. Yang and C. Adachi, *Commun. Mater.*, 2020, **1**, 1–7.

36 A. Kulkarni, F. Ünlü, N. Pant, J. Kaur, C. Bohr, A. K. Jena, S. Öz, M. Yanagida, Y. Shirai and M. Ikegami, *Sol. RRL*, 2021, **5**, 2100077.

37 T. A. P. Phan, N. P. Nguyen, P. H. Nguyen, T. K. Le, T. Van Huynh, T. Lund, D.-H. Tsai, T.-C. Wei, P. T. Nguyen, *et al.*, *Appl. Surf. Sci.*, 2020, **509**, 144878.

38 K. W. Jung, M. R. Sohn, H. M. Lee, I. S. Yang, S. Do Sung, J. Kim, E. W.-G. Diau and W. I. Lee, *Sustainable Energy Fuels*, 2018, **2**, 294–302.

39 I. Chung, B. Lee, J. He, R. P. Chang and M. G. Kanatzidis, *Nature*, 2012, **485**, 486–489.

40 M. O. Reese, S. A. Gevorgyan, M. Jørgensen, E. Bundgaard, S. R. Kurtz, D. S. Ginley, D. C. Olson, M. T. Lloyd, P. Morvillo, E. A. Katz, *et al.*, *Sol. Energy Mater. Sol. Cells*, 2011, **95**, 1253–1267.

41 A. Bou, A. Pockett, D. Raptis, T. Watson, M. J. Carnie and J. Bisquert, *J. Phys. Chem. Lett.*, 2020, **11**, 8654–8659.

42 Y. Seo, S. R. Ha, S. Yoon, S. M. Jeong, H. Choi and D.-W. Kang, *J. Power Sources*, 2020, **453**, 227903.

43 A. K. Baranwal, H. Masutani, H. Sugita, H. Kanda, S. Kanaya, N. Shibayama, Y. Sanehira, M. Ikegami, Y. Numata and K. Yamada, *Nano Convergence*, 2017, **4**, 1–14.

44 S. Hosseini and M. Adelifard, *J. Electron. Mater.*, 2020, **49**, 5790–5800.

45 K. W. Jung, M. R. Sohn, H. M. Lee, I. S. Yang, S. D. Sung, J. Kim, E. Wei-Guang Diau and W. I. Lee, *Sustainable Energy Fuels*, 2018, **2**, 294–302.

46 V. Pecunia, Y. Yuan, J. Zhao, K. Xia, Y. Wang, S. Duhm, L. Portilla and F. Li, *Nano-Micro Lett.*, 2020, **12**, 27.